

See discussions, stats, and author profiles for this publication at: <https://www.researchgate.net/publication/282343359>

# Rotational Orientation Effects in NO(X) + Ar Inelastic Collisions

ARTICLE *in* THE JOURNAL OF PHYSICAL CHEMISTRY A · SEPTEMBER 2015

Impact Factor: 2.69 · DOI: 10.1021/acs.jpca.5b07846

---

READS

25

7 AUTHORS, INCLUDING:



Steven Stolte

Jilin University

236 PUBLICATIONS 4,128 CITATIONS

SEE PROFILE

# 1 Rotational Orientation Effects in NO(X) + Ar Inelastic Collisions

2 M. Brouard,<sup>\*,†</sup> H. Chadwick,<sup>†,§</sup> S. D. S. Gordon,<sup>†</sup> B. Hornung,<sup>†,||</sup> B. Nichols,<sup>†</sup> F. J. Aoiz,<sup>\*,‡</sup>  
 3 and S. Stolte<sup>\*,¶,⊥,#</sup>

4 <sup>†</sup>The Physical and Theoretical Chemistry Laboratory, The Department of Chemistry, University of Oxford, South Parks Road, Oxford  
 5 OX1 3QZ, United Kingdom

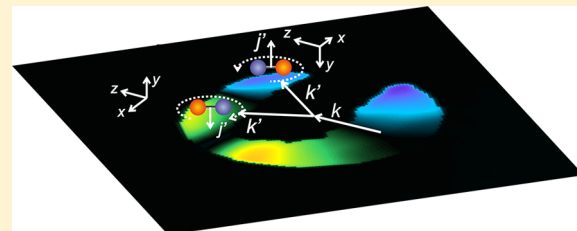
6 <sup>‡</sup>Departamento de Química Física, Facultad de Química, Universidad Complutense, 28040 Madrid, Spain

7 <sup>¶</sup>Institute of Atomic and Molecular Physics, Jilin University, Changchun 130012, China

8 <sup>⊥</sup>Department of Physics and Astronomy, LaserLaB, Vrije Universiteit, Amsterdam, De Boelelaan 1081, 1081 HV Amsterdam, The  
 9 Netherlands

10 <sup>#</sup>Laboratoire Francis Perrin, Bâtiment 522, DRECEM/SPAM/CEA Saclay, 91191 Gif sur Yvette, France

11 **ABSTRACT:** Rotational angular momentum orientation effects in  
 12 the rotationally inelastic collisions of NO(X) with Ar have been  
 13 investigated both experimentally and theoretically at a collision  
 14 energy of 530 cm<sup>-1</sup>. The collision-induced orientation has been  
 15 determined experimentally using a hexapole electric field to select the  
 16  $\epsilon = -1\Lambda$ -doublet level of the NO(X)  $j = 1/2$  initial state. Fully  
 17 quantum state resolved polarization-dependent differential cross  
 18 sections were recorded experimentally using a crossed molecular  
 19 beam apparatus coupled with a (1 + 1') resonance-enhanced  
 20 multiphoton ionization detection scheme and subsequent velocity-map imaging. To determine the NO sense of rotation, the  
 21 probe radiation was circularly polarized. Experimental orientation polarization-dependent differential cross sections are compared  
 22 with those obtained from quantum mechanical scattering calculations and are found to be in good agreement. The origin of the  
 23 collision-induced orientation has been investigated by means of close-coupled quantum mechanical, quantum mechanical hard  
 24 shell, quasi-classical trajectory (QCT), and classical hard shell calculations at the same collision energy. Although there is  
 25 evidence for the operation of limiting classical mechanisms, the rotational orientation cannot be accounted for by QCT  
 26 calculations and is found to be strongly influenced by quantum mechanical effects.



## 27 ■ INTRODUCTION

28 After the rotationally inelastic collision of a diatomic molecule  
 29 with an atom, the molecule can exhibit a preferred sense of  
 30 rotation, i.e., the molecule can preferentially rotate in either a  
 31 clockwise or a counterclockwise direction. This preferred sense  
 32 of rotation corresponds to a positive or negative orientation of  
 33 the final rotational angular momentum,  $j'$ , with respect to the  $y$ -  
 34 axis of the scattering frame, in which the initial and final relative  
 35 velocities,  $k$  and  $k'$ , lie in the  $xz$  plane, with  $k \parallel z$ . The  $k-k'-j'$   
 36 triple vector correlation includes information from both the  
 37 collision-induced alignment (preferred plane of rotation) and  
 38 orientation (sense of rotation) and breaks the constraint  
 39 imposed by the azimuthal symmetry of impact parameters.<sup>1</sup> For  
 40 the NO(X) + Ar system, the collision-induced alignment has  
 41 been found to be well-described by a classical kinematic apse  
 42 model,<sup>2–4</sup> whereas the collision-induced orientation has both  
 43 classical and quantum mechanical (QM) origins,<sup>5–7</sup> and so  
 44 could provide a more sensitive probe of the collision dynamics.  
 45 Collision-induced orientation has been investigated theoreti-  
 46 cally in a number of inelastic<sup>5–9</sup> and reactive scattering  
 47 systems,<sup>10–13</sup> but there have been very few experimental  
 48 investigations.<sup>6,14,15</sup>

49 NO(X) is a  $^2\Pi$  radical with an unpaired electron in a  $\pi^*$   
 50 orbital, giving rise to two spin-orbit manifolds,  $^2\Pi_{1/2}$  and

$^2\Pi_{3/2}$ , separated by approximately 123 cm<sup>-1</sup>. Within each spin-orbit manifold, each rotational level is split into two  $\Lambda$ -doublet sublevels, which are symmetric ( $\epsilon = +1, e$ ) and antisymmetric ( $\epsilon = -1, f$ ) combinations of the  $+\Omega$  and  $-\Omega$  wave functions. For low  $j$  states, the  $\Lambda$ -doublet sublevels are nearly degenerate but differ in parity, given by  $p = \epsilon(-1)^{j-1/2}$ . On nonlinear approach of an Ar atom to the NO(X) molecule, the degeneracy of the  $^2\Pi$  state is lifted, resulting in two potential energy surfaces of  $A'$  and  $A''$  symmetry. In the case of Hund's case (a) molecules, it has been shown<sup>16,17</sup> that the spin-orbit conserving transitions can be considered to take place on a summed potential

$$V_{\text{sum}}(R, \gamma) = \frac{1}{2}[V_A(R, \gamma) + V_{A''}(R, \gamma)] \quad (1)$$

while spin-orbit changing collisions are coupled by a difference potential

**Special Issue:** Dynamics of Molecular Collisions XXV: Fifty Years of Chemical Reaction Dynamics

**Received:** August 12, 2015

**Revised:** September 26, 2015

$$V_{\text{diff}}(R, \gamma) = \frac{1}{2} [V_{A''}(R, \gamma) - V_{A'}(R, \gamma)] \quad (2)$$

66 Here,  $V_{A'}$  and  $V_{A''}$  are the potential energy surfaces (PESs) for  
 67 the two lowest-lying electronic states of  $\text{NO}(X) + \text{Ar}$ ;  $R$  is the  
 68 distance between the Ar atom and the center of mass of the  
 69 diatom; and  $\gamma$  is the angle between  $\mathbf{R}$  and the NO bond axis,  $\mathbf{r}$ .  
 70 The  $\text{NO}(X) + \text{Ar}$  system has been the basis of numerous  
 71 experimental and theoretical investigations. Many of these  
 72 studies have focused on determining the integral cross  
 73 sections<sup>18,19</sup> as well as lower-order vector correlations, such  
 74 as the  $\mathbf{k}\cdot\mathbf{k}'$  correlation, embodied in the differential cross  
 75 section.<sup>18,20–31</sup> Parity-dependent effects have been observed in  
 76 both the integral<sup>19</sup> and differential cross sections.<sup>26–31</sup> More  
 77 recently, the collision-induced alignment in the  $\text{NO}(X) + \text{Ar}$   
 78 system has been investigated experimentally<sup>4,32</sup> and theoret-  
 79 ically,<sup>3</sup> and the classical kinematic apse model was found to  
 80 largely explain the observed rotational alignment. Lorenz et al.  
 81 demonstrated that the rotational orientation of the  $\text{NO}(X)$   
 82 molecule after collisions with Ar could be determined using  
 83 circularly polarized light; however, in these experiments the  
 84 initial  $\Lambda$ -doublet level of the  $\text{NO}(X)$  was not selected prior to  
 85 the collision.<sup>6</sup> It was found that the experimentally observed  
 86 orientation oscillated with scattering angle between positive and  
 87 negative values for low and medium rotational excitation, an  
 88 effect that was reproduced by quantum mechanical calculations,  
 89 but not by classical models.<sup>6</sup> As an antecedent of the present  
 90 study, the collision-induced alignment and orientation of NO in  
 91 the  $\text{NO}(X) + \text{Kr}$  system was investigated using the same  
 92 experimental method as that presented here.<sup>15</sup> However, that  
 93 study was restricted to the lowest  $\Delta j$  transitions and did not  
 94 observe oscillations with scattering angle because only a small  
 95 angular range was recorded.

96 In this paper, the collision-induced orientation of the  $\text{NO}(X)$   
 97 + Ar system is investigated experimentally and theoretically. We  
 98 present here a comprehensive set of fully  $\Lambda$ -doublet state  
 99 resolved collision-induced orientation data for the first time.  
 100 We also discuss in detail the mechanisms responsible for  
 101 collision-induced orientation and provide evidence that the  
 102 observed orientation has a significant quantum mechanical  
 103 contribution, which cannot be accounted for by classical  
 104 calculations. **Methods** contains details of the experimental  
 105 methods and theoretical calculations used in the paper.  
 106 Experimentally determined collision-induced orientation for  
 107 fully  $\Lambda$ -doublet resolved collisions of  $\text{NO}(X) + \text{Ar}$  is presented  
 108 in **Experimental Results**, where the experimentally determined  
 109 orientation moments are also compared with corresponding  
 110 quantum mechanical calculations. In **Rotational Orientation in**  
 111 **Classical Collisions and Quantum Mechanical Collisions**, the  
 112 results of the classical and quantum mechanical calculations are  
 113 compared and discussed. The main findings of the paper are  
 114 then summarized in **Conclusions**.

## 115 ■ METHODS

116 **Experimental Methods.** The experimental apparatus has  
 117 been fully described in previous work,<sup>26,33</sup> and only brief details  
 118 will be presented here. The fully quantum state resolved  
 119 polarization-dependent differential cross sections (PDDCSs)  
 120 were recorded experimentally using a crossed molecular beam  
 121 apparatus coupled with a  $(1 + 1')$  resonance-enhanced  
 122 multiphoton ionization (REMPI) detection scheme and  
 123 subsequent velocity-map imaging.<sup>34</sup> The NO molecular  
 124 beam was generated using a pulse General valve operating at

10 Hz with a backing pressure of 3 bar. The NO was seeded at 125  
 16% in argon to aid adiabatic cooling. The molecular beam 126  
 then passed through two skimmers and entered the hexapole 127  
 electric field, which exploited the Stark effect to select the  $|j = 128$   
 $0.5, \Omega = 0.5, \epsilon = -1\rangle$  quantum state and focused it into the 129  
 interaction region. The NO molecular beam was then 130  
 intersected perpendicularly by a beam of Ar atoms. The Ar 131  
 beam consisted of pure argon and was produced by a General 132  
 valve operating at 5 Hz to allow shot-to-shot subtraction of any 133  
 unscattered NO signal.<sup>134</sup>

To allow state-selective detection of the scattered NO 135  
 products, a  $(1 + 1')$  REMPI detection scheme was employed.<sup>136</sup> 90% of the 308 nm output of a XeCl excimer laser was used to 137  
 pump a tunable dye laser. Coumarin 450 dye in methanol was 138  
 used to achieve lasing at around 452 nm. This was then 139  
 frequency-doubled to wavelengths around 226 nm, which could 140  
 be tuned to the particular  $\text{NO}(A \leftarrow X)$  rotational transition of 141  
 interest. The 226 nm beam was directed through a Rochon 142  
 polarizer, photoelastic modulator, and  $\lambda/4$  plate to generate 143  
 alternating right and left circularly polarized light. To determine 144  
 the sense of NO rotation in the plane defined by the molecular 145  
 beams,<sup>15</sup> the probe laser was directed perpendicularly through 146  
 this plane, passing through a 4 mm diameter hole in the repeller 147  
 plate, as depicted in **Figure 1**. The remaining 10% of the 308 148 fl

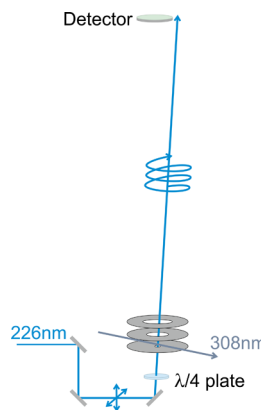


Figure 1. Schematic of the experimental setup of the interaction volume. The excitation laser is directed perpendicular to the plane defined by the molecular beams and toward the detector.<sup>6</sup> To avoid hitting the detector, the laser was directed off-axis by approximately 2°. The circularly polarized light is generated using a photoelastic modulator and quarter-wave plate.

nm laser, used to ionize the excited  $\text{NO}(A)$  molecules,<sup>149</sup> intersected the molecular beams at 45° in the plane defined 150 by the molecular beams. Velocity-map imaging was then 151 employed to image the  $\text{NO}^+$  ions.<sup>152</sup>

In the following, the experimental images are presented as 153 the normalized difference  $(I_L - I_R)/(I_L + I_R)$  of the individual 154 DCS images recorded using right circularly polarized light ( $I_R$ ) 155 and left circularly polarized light ( $I_L$ ).<sup>36</sup> This minimizes flux- 156 density and differential cross section effects on the observed 157 orientation.<sup>4,32</sup> The experimental images were then fit in 158 Fourier moment space using an iterative fitting method that has 159 been fully described previously.<sup>4,37</sup><sup>160</sup>

**Polarization-Dependent Differential Cross Sections.** The 161 results presented here are shown in the scattering frame, in 162 which the relative velocity,  $\mathbf{k}$ , defines the direction of the  $z$  axis.<sup>163</sup> The final relative velocity after the collision,  $\mathbf{k}'$ , is taken to lie in 164

165 the  $xz$  plane, with  $x > 0$ , while the  $y$  axis is chosen to have a  
166 right-handed frame of reference.

167 The classical probability that a particle is scattered through  
168 an angle,  $\theta$ , with its rotational angular momentum,  $\mathbf{j}'$ , pointing  
169 in a direction ( $\theta_{j'}$ ,  $\phi_{j'}$ ) is given by<sup>12</sup>

$$P(\cos \theta, \cos \theta_{j'}, \phi_{j'}) = \sum_{kq} \frac{2k+1}{4\pi} \left( \frac{2\pi}{\sigma} \frac{d\sigma_{kq}}{d\omega} \right) C_{kq}^*(\theta_{j'}, \phi_{j'}) \quad (3)$$

170 where the  $C_{kq}^*(\theta_{j'}, \phi_{j'})$  are the complex conjugates of the  
171 modified spherical harmonics and the expansion coefficients,  
172  $n_q^{(k)}(\theta) \equiv (2\pi/\sigma)d\sigma_{kq}/d\omega$ , are the normalized PDDCSs, which  
173 are the polarization moments that characterize the distribution  
174 of the final rotational angular momentum of the scattered  
175 particles as a function of scattering angle.<sup>12</sup>

176 Quantum mechanically, the un-normalized PDDCSs can be  
177 calculated according to<sup>38</sup>

$$\frac{d\sigma_{kq}}{d\omega} = \frac{1}{2j+1} \sum_{m, m'_1, m'_2} f_{jm\Omega\epsilon \rightarrow j'm'_1\Omega'\epsilon'}(\theta) f_{jm\Omega\epsilon \rightarrow j'm'_2\Omega'\epsilon'}^*(\theta) \langle j'm'_1, kq | j'm'_2 \rangle \quad (4)$$

178 where  $f_{jm\Omega\epsilon \rightarrow j'm'_1\Omega'\epsilon'}(\theta)$  is the scattering amplitude for the  
179 transition with the indicated quantum numbers,  $\sigma$  the integral  
180 cross section for the transition, and  $\langle j'm'_1, kq | j'm'_2 \rangle$  a Clebsch–  
181 Gordan coefficient. The normalized PDDCS is given by<sup>38</sup>

$$n_q^{(k)} = \frac{2\pi}{\sigma} \frac{d\sigma_{kq}}{d\omega} = \frac{2\pi}{\sigma} \frac{1}{2j+1} \sum_{m, m'_1, m'_2} f_{jm\Omega\epsilon \rightarrow j'm'_1\Omega'\epsilon'}(\theta) f_{jm\Omega\epsilon \rightarrow j'm'_2\Omega'\epsilon'}^*(\theta) \quad (5)$$

182 The renormalized PDDCSs are then given by<sup>38</sup>

$$\rho_q^{(k)}(\theta) = \frac{(d\sigma_{kq}/d\omega)}{(d\sigma_{00}/d\omega)} = \frac{n_q^{(k)}}{n_0^{(0)}} = \frac{\sum_{m, m'_1, m'_2} f_{jm\Omega\epsilon \rightarrow j'm'_1\Omega'\epsilon'}(\theta) f_{jm\Omega\epsilon \rightarrow j'm'_2\Omega'\epsilon'}^*(\theta) \langle j'm'_1, kq | j'm'_2 \rangle}{\sum_{m, m'} |f_{jm\Omega\epsilon \rightarrow j'm'\Omega'\epsilon'}(\theta)|^2} \quad (6)$$

183 ( $d\sigma_{00}/d\omega$ ) is the  $k = 0$ ,  $q = 0$  PDDCS, which is equal to the  
184 differential cross section and quantifies the angular distribution  
185 of the scattered products.

186 Finally, the integral polarization parameters (PPs) can be  
187 obtained upon integration of the normalized PDDCS over the  
188 scattering angle. Thus, specifically for the orientation PP, we  
189 have

$$a_{1-}^{\{1\}} = \int_{-1}^{+1} n_{1-}^{\{1\}}(\theta) d\cos \theta \quad (7)$$

190 The limits of the PP coincide with those of the renormalized  
191 PDDCS and are function of the  $j'$  value.

192 The PDDCSs and PPs are in general complex, and so the real  
193 PDDCSs  $n_{q\pm}^{(k)}(\theta)$  and PP  $a_{q\pm}^{\{k\}}$  are obtained using the Hertel–  
194 Stoll convention.<sup>12,39</sup>

195 As will be seen in the following, it is also convenient to define  
196 the classical polarization-dependent partial cross section  
197 (PDPCS) as

$$\sigma_q^{\{k\}}(b) = 2\pi b P_q^{\{k\}}(b) \quad (8)$$

198 where  $P_q^{\{k\}}(b)$  is a polarization-dependent opacity function. For  
199  $k = q = 0$

$$\sigma_0^{\{0\}}(b) = 2\pi b P(b) \quad (9)$$

200 with

$$\int_0^{b_{\max}} \sigma_0^{\{0\}}(b) db = \sigma \quad (10)$$

201 Of more interest is the *normalized* polarization-dependent  
202 partial cross section (n-PDPCS):

$$p_q^{\{k\}}(b) = \frac{2\pi}{\sigma} b P_q^{\{k\}}(b) = \frac{\sigma_q^{\{k\}}(b)}{\sigma} \quad (11)$$

203 It is easily shown that the integral polarization parameters,  $a_q^{\{k\}}$ ,  
204 are related to the n-PDPCS via:

$$a_q^{\{k\}} = \frac{2\pi}{\sigma} \int_0^{b_{\max}} b p_q^{\{k\}}(b) db = \int_0^{b_{\max}} p_q^{\{k\}}(b) db \quad (12)$$

205 **Classical Hard Shell Calculations.** Spin–orbit conserving  
206 transitions take place on the  $V_{\text{sum}}(R, \gamma)$  potential energy surface  
207 in the Hund's case (a) limit.<sup>16,40</sup> Therefore, the quasi-classical  
208 trajectory (QCT) and classical hard shell calculations were  
209 carried out on the  $V_{\text{sum}}(R, \gamma)$  potential energy surface. Except  
210 for an attractive well of approximately  $-110$  cm<sup>−1</sup> depth at  
211 larger interparticle separations, the potential is strongly  
212 repulsive. It is thus reasonable to model the  $V_{\text{sum}}(R, \gamma)$  potential  
213 with a hard shell potential, i.e., a potential which is infinite  
214 inside a contour and zero outside of that at the present collision  
215 (here also total) energy of 530 cm<sup>−1</sup>.<sup>7,41</sup> The comparison of the  
216 results obtained on this hard shell PES with calculations  
217 employing the full or modified “soft” repulsive PESs<sup>41</sup> (see  
218 [QCT Calculations](#)) helps to identify the role of different parts  
219 of the potential in determining the collision-induced rotational  
220 orientation. The two-dimensional (2D) hard shell contour, with  
221  $C_{\infty\infty}$  symmetry, was obtained as the intersection between the  
222  $V_{\text{sum}}(R, \gamma)$  potential and the collision energy.<sup>7</sup> The method of  
223 Beck and Ross was adopted in order to carry out the hard shell  
224 calculations.<sup>42–45</sup> The details of the Monte Carlo calculations  
225 were described in ref 7. A single batch of  $7 \times 10^6$  inelastic  
226 trajectories was analyzed to obtain the PDDCSs and partial  
227 cross sections presented in [Results and Discussion](#).

228 **QCT Calculations.** The details of the QCT calculations  
229 employed in this work are described elsewhere,<sup>7,25,46</sup> and only  
230 those aspects that are specific to this work are described here.  
231 The trajectory calculations employed the  $V_{\text{sum}}(R, \gamma)$  of  
232 Alexander.<sup>19</sup> The classical equations of motions were solved  
233 while the N–O interatomic distance was kept fixed using the  
234 method of Lagrange multipliers. The square of the classical  
235 angular momentum was equated to  $j'(j'+1)\hbar^2$ , and the values  
236 of  $j'$  were then rounded to the nearest integer. The maximum  
237 value of the impact parameter was determined as 6.3 Å, beyond  
238 which no trajectories lead to inelastic collisions.

239 To ascertain the effects of the finite range repulsion in the  
240 absence of the attractive features of the potential, a “soft”  
241 potential was constructed. This “soft” potential is purely  
242 repulsive, the attractive parts having been removed using an  
243 appropriate damping function:<sup>41</sup>

$$f(R, R_0, R_{\text{shift}}, \alpha) = 1 - \frac{1}{1 + \exp(-\alpha(R - R_0 + R_{\text{shift}}))} \quad (13)$$

where  $\alpha$ ,  $R_0$ ,  $R_{\text{shift}} > 0$ , and  $\alpha$  determines the steepness of the function.  $R_{\text{shift}}$  shifts the inflection point of  $f(R, R_0, R_{\text{shift}}, \alpha)$  toward smaller  $R$ , so that scaled potentials drop below a predefined small value of  $\epsilon \times E_{\text{coll}}$  at a distance of  $R_0$ .  $\epsilon$  was chosen to be  $10^{-2}$ .  $R_0$  is the contour of the  $V_{\text{sum}}(R, \gamma)$  PES at zero collision energy. As such, it depends on  $\gamma$ , the Jacobi angle.

A comparison of the soft and full potentials can be found in ref 41.

The sum and difference PESs can then be written as

$$\tilde{V}_{\text{sum}}(R, \gamma_i) = V_{\text{sum}}(R, \gamma_i) f(R_i, R_{0,i}, R_{\text{shift},i}, \alpha_i) \quad (14)$$

$$\tilde{V}_{\text{diff}}(R, \gamma_i) = V_{\text{diff}}(R, \gamma_i) f(R_i, R_{0,i}, R_{\text{shift},i}, \alpha_i) \quad (15)$$

where the index,  $i$ , runs over the Jacobi angles at which the original  $A'$  and  $A''$  PESs were calculated.<sup>19</sup> In this manner it is possible to modify both  $V_{\text{sum}}(R, \gamma)$  and  $V_{\text{diff}}(R, \gamma)$  so that they remain the half sum and half difference of the  $V_{A'}$  and  $V_{A''}$  potentials. In the present calculations,  $\alpha_i$  was set in the 1.0–5.0 bohr<sup>-1</sup> range and  $R_{\text{shift},i}$  in the 1.0–0.50 bohr range. The scattering results are quite similar within these ranges of parameters.

**QM Hard Shell Calculations.** The method of Bosanac and Petrović<sup>47,48</sup> was used to solve the quantum mechanical scattering problem of a pointlike atom and a hard shell.<sup>7</sup> The 2D hard shell contour was identical to that used in the classical hard shell calculations. Rotational states up to  $j = 23$  and partial waves up to  $J = 100$  were included in the scattering wave function to achieve convergence.<sup>7</sup>

**QM Close-Coupled Calculations.** Full nonadiabatic close-coupled calculations were carried out on the  $V_{\text{sum}}(R, \gamma)$  and  $V_{\text{diff}}(R, \gamma)$  coupled-cluster singles, doubles, perturbative triples (CCSD(T)) PESs of Alexander<sup>19</sup> using the Hibridon suite of codes.<sup>49</sup> The PESs were calculated with the N–O bond length kept fixed at its equilibrium value.<sup>19</sup> As a consequence, the vibrational degree of freedom is ignored in the calculations presented in this paper. The collision energy was set to 530 cm<sup>-1</sup> ( $\approx 66$  meV), which corresponds to the mean experimental collision energy. Rotational levels up to  $j' = 20.5$ , both  $\Lambda$ -doublet levels ( $\epsilon = -1,+1$ ) and spin-orbit manifolds ( $\Omega = 0.5, 1.5$ ) were included in the scattering wave function. The maximum partial wave was set to  $J = 160.5$  to achieve convergence, which corresponds to a classical impact parameter of 6.8 Å. In the case of “soft” potential calculations, both  $V_{\text{sum}}(R, \gamma)$  and  $V_{\text{diff}}(R, \gamma)$  were scaled according to eqs 13 and 14. In addition to the open shell calculations, closed shell scattering calculations were carried out on the  $V_{\text{sum}}$  PES, in which the NO(X) was treated as a closed shell molecule in order to provide a direct comparison to QCT and QM hard shell results.

## RESULTS AND DISCUSSION

**Experimental Results. Images and Experimental PDDCs.** Figure 2 shows the experimental difference ( $I_L - I_R$ ), normalized difference ( $(I_L - I_R)/(I_L + I_R)$ ), along with the individual DCS images recorded using right- and left-handed circularly polarized light (RCP and LCP) for a range of spin-orbit conserving  $f-f$  transitions. The NO is probed using  $R_{21} \uparrow$  branch excitation; therefore, RCP preferentially detects molecules rotating in an anticlockwise direction in the plane of the molecular beams, such that  $j'$  is directed antiparallel to the laser propagation axis. Molecules rotating in a clockwise direction are preferentially detected with LCP. Therefore,

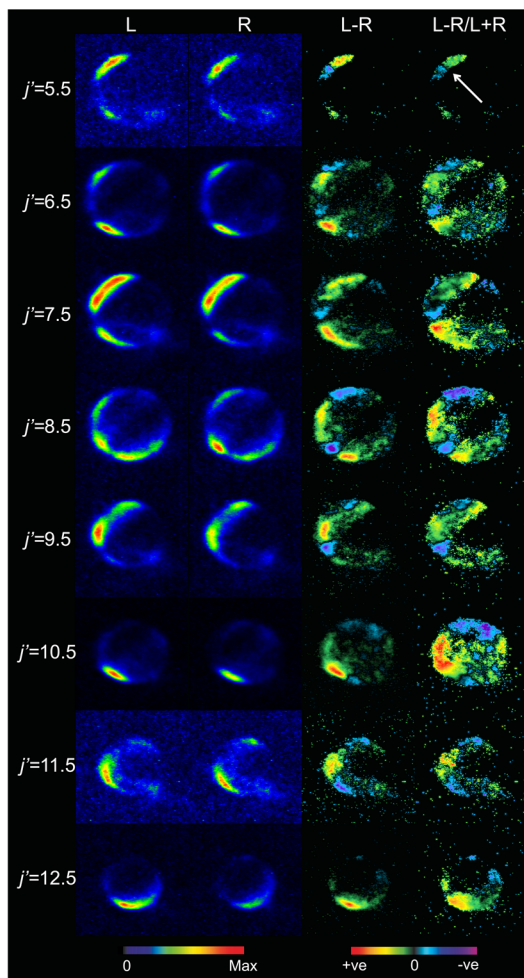


**Figure 2.** Experimental difference ( $I_L - I_R$ ), normalized difference ( $(I_L - I_R)/(I_L + I_R)$ ) and individual  $I_L$  and  $I_R$  DCS images for transitions between  $|\Omega = 0.5, j = 0.5, f\rangle \rightarrow |\Omega' = 0.5, j', f\rangle$ , where  $j' = 5.5-12.5$ . The direction of the relative velocity is shown by a white arrow in the top right image.

negative intensity indicates an anticlockwise rotation in the plane defined by the molecular beams and positive intensity corresponds to clockwise rotation.<sup>6,36</sup>

The difference and normalized difference images show a sign inversion when reflected in the perpendicular plane containing the relative velocity (indicated by a white arrow). This can be understood by considering the direction of the scattering frame  $y$ -axis for different parts of the image. Figure 3 illustrates the angular momentum orientation after a collision for  $\Delta j = 12.5$ . Trajectories that result in scattering to the slow side of the

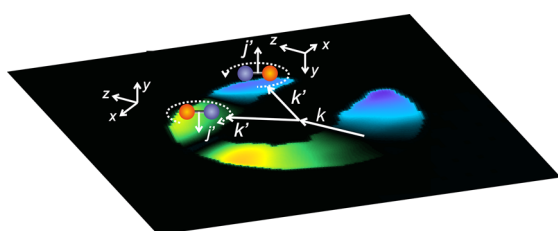


**Figure 3.** Illustration of the rotational orientation after a collision of NO(X) with Ar resulting in the  $j' = 12.5, f$  state. The  $x$ ,  $y$ , and  $z$  axes of the scattering frame are shown for each side of the image.

324 image (to the bottom left of the relative velocity) rotate in a  
 325 clockwise direction and show positive intensity. Because the  
 326 orientation is defined relative to the scattering frame  $y$ -axis, this  
 327 corresponds to negative orientation (i.e.,  $j'$  is oriented  
 328 antiparallel to the scattering frame  $y$ -axis). Trajectories that  
 329 scatter through the same angle,  $\theta$ , into the fast side of the image  
 330 (top right of the relative velocity) rotate in an anticlockwise  
 331 direction in the laboratory frame and so are preferentially  
 332 detected by RCP light and are shown by negative intensity.  
 333 Although these molecules have the opposite sense of rotation in  
 334 the plane defined by the molecular beams, the scattering frame  
 335 has been inverted because of the change in direction of  $k'$ ;  
 336 therefore, the orientation in the scattering frame is still negative.  
 337 In areas of the experimental DCS images where the signal  
 338 intensity is low, such as the center of the image, it is not  
 339 possible to gain orientation information. In some DCS images  
 340 (for example, for  $j' = 11.5$ ), experimental background can be  
 341 seen in the backward scattered direction (see Figure 2).  
 342 Because the excitation laser was passed through a small hole in  
 343 the charged repeller plate, it is possible that slight clipping of  
 344 the plate by the beam could result in ejection of electrons from  
 345 the charged plate. These electrons may have been able to ionize  
 346 Ar from the secondary beam and so caused increased  
 347 experimental background signal in the backward scattered  
 348 direction.

349 Figure 4 displays the experimental and fitted normalized  
 350 difference images. Agreement between the fitted and

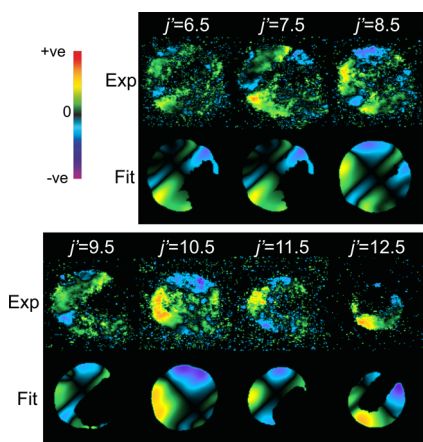


Figure 4. Experimental (top row) and fitted (bottom row) normalized difference ion images  $(I_L - I_R)/(I_L + I_R)$  for spin-orbit conserving  $f-f$  transitions.

351 experimental images is good, lending confidence to the  
 352 conclusion that a sufficient number of moments has been  
 353 applied in the fitting process to reproduce the experimental  
 354 data. A threshold was applied to the experimental and fitted  
 355 images, such that where the experimental intensity, or QM  
 356 DCSs are small, the normalized difference image is set to zero.  
 357 Experimentally determined  $\rho_{1-}^{(1)}(\theta)$  orientation moments are  
 358 shown in the middle column of Figure 5, along with those  
 359 obtained from QM calculations. The agreement between the  
 360 experimental and theoretical  $\rho_{1-}^{(1)}(\theta)$  PDDCSs is rather good.  
 361 The main disagreements are due to lack of experimental  
 362 intensity in the image, for example in the forward scattered  
 363 direction  $j' = 12.5f$ . The magnitude of the positive orientation  
 364 in the experimental fits is also slightly less than the QM  
 365 calculation for sideways scattering in  $j' = 7.5$  and  $j' = 9.5$  ( $\Delta j =$

366 7 and 9, respectively). In the case of the collision-induced 366  
 367 rotational alignment of NO by Kr,<sup>37</sup> it was proposed that 367  
 368 secondary inelastic collisions were responsible for a slight 368  
 369 reduction in collision-induced alignment moments compared 369  
 370 with theory. This does not appear to be the issue with the 370  
 371 present orientation measurements, because depolarizing 371  
 372 collisions would be likely to affect both positive and negative 372  
 373 orientation. In contrast to the alignment measurements in NO 373  
 374 + Kr, in the case of NO + Ar, the negative orientation is not 374  
 375 significantly underestimated. This seems to rule out secondary 375  
 376 collisions as a potential explanation for the discrepancy between 376  
 377 theory and experiment for  $j' = 7.5$  and  $j' = 9.5$ .

A positive value of  $\rho_{1-}^{(1)}(\theta)$  indicates that the rotational 378  
 379 angular momentum,  $j'$ , lies preferentially parallel to the 379  
 380 scattering frame along the  $+y$  semiaxis, while a negative value 380  
 381 corresponds to  $j'$  along  $-y$ . For the lowest  $j'$  transition 381  
 382 recorded, the experimental and QM  $\rho_{1-}^{(1)}(\theta)$  PDDCSs oscillate 382  
 383 between positive and negative values over the entire angular 383  
 384 region. As  $j'$  increases, the frequency of these oscillations can be 384  
 385 seen to decrease, and  $\rho_{1-}^{(1)}(\theta)$  becomes negative over a larger 385  
 386 angular range. As will be discussed in the following sections, the 386  
 387 orientation becomes increasingly negative because of the more 387  
 388 repulsive nature of the collisions. The decrease in frequency of 388  
 389 the oscillations observed in the experimental and QM PDDCSs 389  
 390 has been rationalized in terms of the outgoing de Broglie 390  
 391 wavelength for the system.<sup>7</sup> As the rotational excitation of the 391  
 392 NO increases, the final relative velocity of the system decreases, 392  
 393 resulting in a corresponding increase in the outgoing de Broglie 393  
 394 wavelength. The observed oscillatory behavior of the  $\rho_{1-}^{(1)}(\theta)$  394  
 395 PDDCS is in agreement with previous measurements of 395  
 396 collision-induced orientation in the NO(X) + Ar system by 396  
 397 Lorenz et al.,<sup>6</sup> although the exact details of the oscillations differ 397  
 398 due to the initial  $\Lambda$ -doublet selection in the current work.

Experimental and QM normalized angular distributions,  $P(\theta)$  399  
 (that is, the normalized DCSs,  $n_0^{(0)}(\theta)$ ), are also shown in the 400  
 first column of Figure 5. The experimental normalized (11-) 401  
 orientation PDDCSs,  $n_{1-}^{(1)}(\theta)$ , are calculated multiplying the 402  
 renormalized  $\rho_{1-}^{(1)}(\theta)$  PDDCSs by the normalized angular 403  
 distributions. The third column of Figure 5 displays the 404  
 experimental and QM  $n_{1-}^{(1)}(\theta)$  PDDCSs. Again, the agreement 405  
 between experiment and theory is good, reflecting that found 406  
 for the angular distributions and  $\rho_{1-}^{(1)}(\theta)$  PDDCSs.

A comparison of QM and QCT simulations is shown in 408  
 Figure 6, along with the corresponding experimental images. A 409  
 threshold has been applied to the experimental, QM, and QCT 410  
 simulated images such that where the experimental intensity is 411  
 low or the calculated DCS drops below a specified value, the 412  
 normalized difference image is set to zero. The QM simulations 413  
 reproduce the features seen experimentally, including the sign 414  
 changes in the orientation.

However, it is clear that the QCT simulations are unable to 416  
 417 reproduce the collision-induced orientation observed in the 417  
 experimental images. The dominant feature in the QCT 418  
 simulations is the intense peak in the orientation predicted in 419  
 the forward scattered direction, which increases in intensity and 420  
 becomes broader as the rotational excitation increases. The 421  
 peak in the orientation is seen clearly in the QCT renormalized 422  
 $\rho_{1-}^{(1)}(\theta)$  PDDCSs (the column in Figure 6), which shows 423  
 negative peaking orientation at scattering angles around  $\theta \approx 0^\circ$  424  
 for  $\Delta j = 6$  and  $\theta \approx 30^\circ$  for  $\Delta j = 12$ . The peak in the QCT 425  
 predicted orientation is also clearly observed as an intense 426  
 orientation feature in the QCT simulated normalized difference 427  
 images (third column of Figure 6). To the left of the relative 428

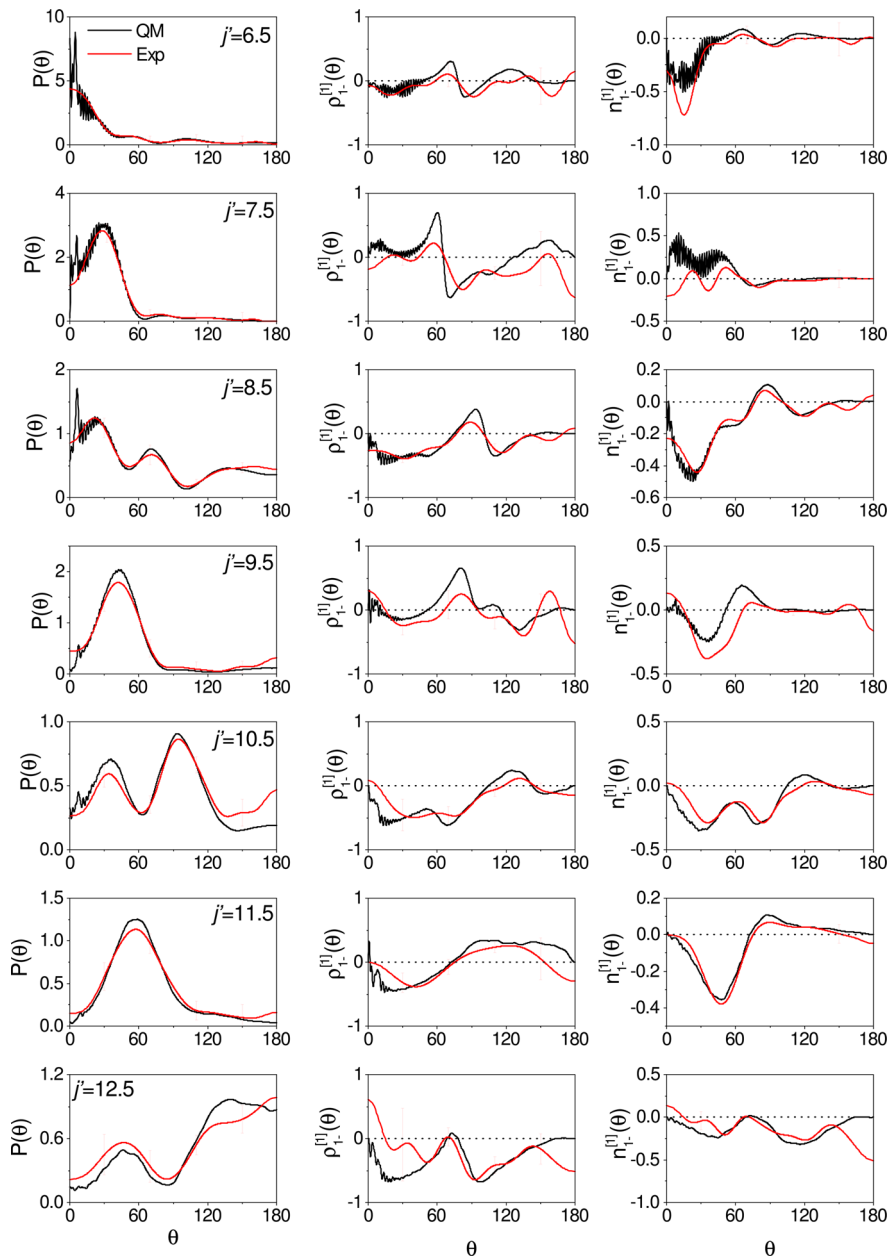


**Figure 5.** Experimentally determined (red line) and QM calculated (black line) normalized angular distributions (left column), renormalized  $\rho_{1-}^{(1)}(\theta)$  PDDCSs (center column), and normalized  $n_{1-}^{(1)}(\theta)$  PDDCSs (right column). The data are for spin–orbit conserving  $f$ – $f$  transitions. The error bars on the experimental data represent the 95% confidence limits.

429 velocity, the intense peak in the QCT predicted normalized  
430 difference images is positive, indicating rotation of the NO in a  
431 clockwise direction in the lab frame and therefore negative  
432 orientation of  $j'$  with respect to the scattering frame  $y$ -axis, as  
433 shown in Figure 3. This propensity for negative orientation in  
434 the forward scattered direction is also seen in the experimental  
435 and QM images for  $j' \geq 8.5$ ; however, it is much less  
436 pronounced than in the QCT simulations, as is evident from  
437 comparison of the QM and QCT renormalized  $\rho_{1-}^{(1)}(\theta)$   
438 PDDCSs shown in Figure 6. Again, negative orientation can  
439 be seen in both sets of calculations at small scattering angles;  
440 however, the agreement between the QM and QCT  
441 calculations is far from quantitative, with oscillations observed  
442 in the QM calculations that are not reproduced by the classical  
443 calculations.

**Experimental Integral Orientation Moments.** Experimentally determined, QM, and QCT calculated  $a_{1-}^{(1)}$  integral orientation moments, which are obtained by integrating the corresponding normalized PDDCSs, eq 7, are compared in Figure 7. The experimental and quantum mechanical moments are in good agreement, although some discrepancies for  $\Delta j = 7$  and  $\Delta j = 9$  can be seen, perhaps due to the disagreement in the  $\rho_{1-}^{(1)}(\theta)$  in the region of the sharp feature at sideways scattered angles (around 90°), as seen in Figure 5. Both the experimental and QM data show the parity-dependent alternations with rotational state, which are not observed in the QCT calculations. All three sets of data show the same general trend, with the orientation moment becoming more negative with increasing  $\Delta j$  as a consequence of the increasing repulsive nature of the collisions. The good agreement between the general trend of the QCT and experimental and QM data

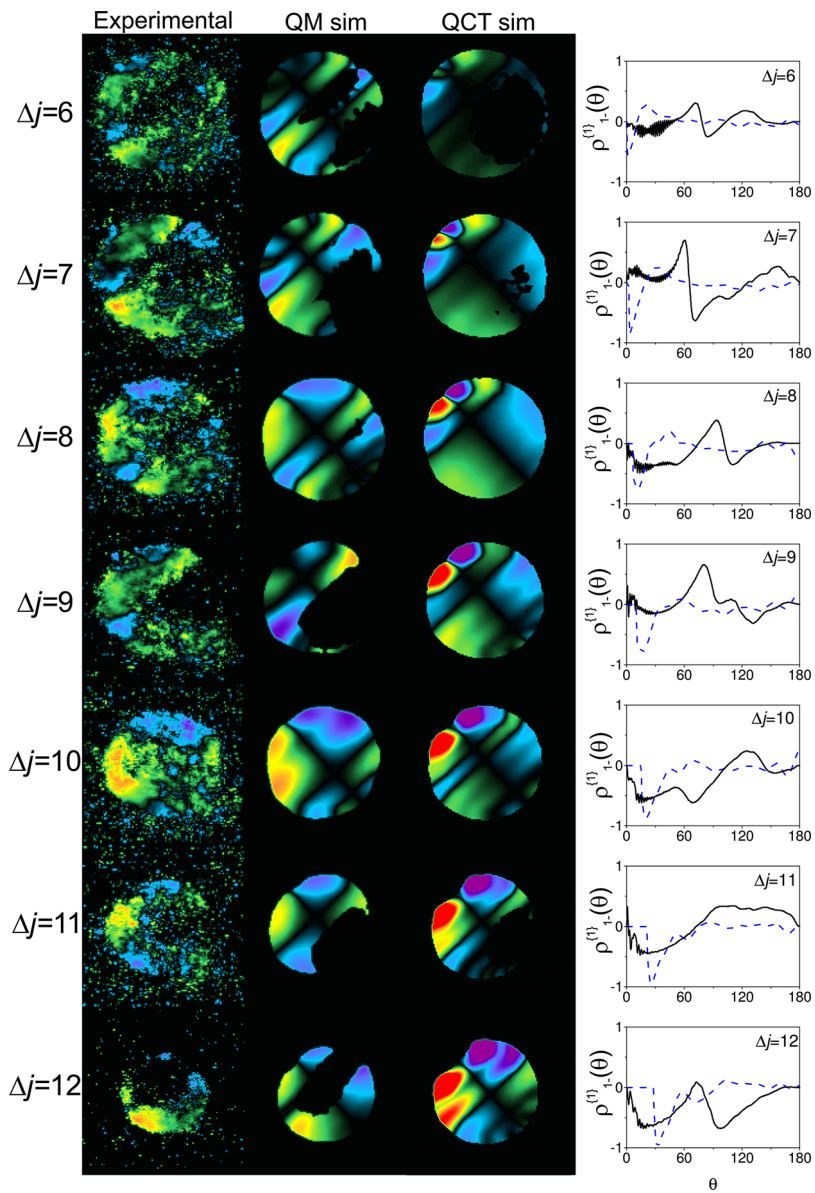


**Figure 6.** Experimental, open shell QM simulated, and closed shell QCT simulated normalized difference  $(I_L - I_R)/(I_L + I_R)$  images for transitions between  $\Delta j = 6-12$ . The experimental images and QM simulations are for spin-orbit conserving  $f-f$  states. The corresponding QM and QCT  $\rho_{1-}^{(1)}(\theta)$  moments from open shell QM (black solid line) and closed shell QCT calculations (blue dashed line) are shown in the fourth column.

460 confirm that the limiting attractive and repulsive classical  
461 mechanisms, which will be discussed in the following sections,  
462 also play a role in the quantum mechanical scattering of NO(X)  
463 by Ar.

464 **Rotational Orientation in Classical Collisions.** *Classical*  
465 *Hard Shell Calculations.* The simplest model in which to  
466 consider collision-induced orientation is that of a classical hard  
467 shell collision. It has previously been found that there cannot be  
468 net rotational orientation in *classical* single-encounter collisions  
469 of a hard shell and a structureless atom.<sup>45</sup> These encounters  
470 take place at an infinitely small point on the molecular surface  
471 in an infinitely short interaction time. Under these circum-  
472 stances, the body fixed frame components of the final rotational  
473 angular momentum,  $j'$ , are determined by the point-of-contact,  
474 the surface normal at this point, and by the projection of the  
475 initial relative linear momentum onto the surface normal (see  
476 Figure 8).<sup>42</sup> Therefore, there is cylindrical symmetry of the  
477 trajectories about the surface normal, which leads to identical  $j'$

478 in the body fixed frame. However, the scattering frame will be  
479 different for each of these collisions in the body fixed frame  
480 because the scattering frame is defined by the initial and final  
481 relative velocities. Those collisions that are related by a rotation  
482 through an angle of  $\pi$  about the surface normal are associated  
483 with scattering frames whose  $y$ -axis are antiparallel. Therefore,  
484 the two rotational orientations will be equal with respect to  
485 their modulus, but have different signs. Thus, although each  
486 individual collision results in a specific sense of rotation of the  
487 molecule, for every impact that results in a clockwise rotation,  
488 an equivalent encounter at the same point on the molecule,  
489 leading to the same scattering angle and  $\Delta j$ , will induce equal  
490 and opposite anticlockwise rotation; hence, no net orientation  
491 can take place. It is worth noting that one of the equivalent  
492 trajectories is usually associated with small impact parameters  
493 and shallow incident Jacobi angles with respect to molecular  
494 bond axis, while the other is characterized by larger impact  
495 parameters and Jacobi angles closer to  $90^\circ$ , as shown in Figure 495

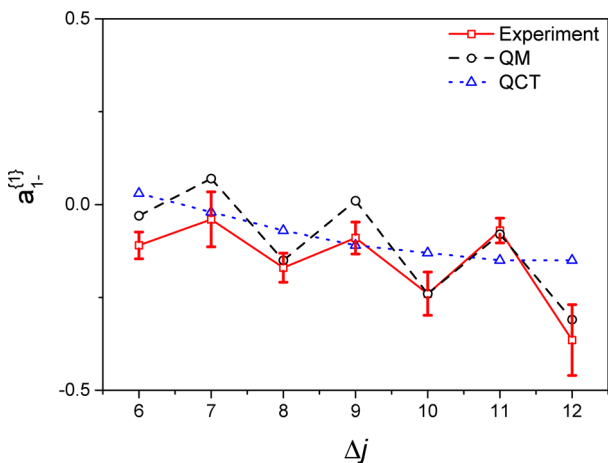


**Figure 7.** Comparison of experimentally determined (red squares) integral polarization parameters,  $a_{1-}^{(1)}$ , with their QM and QCT counterparts for  $\Delta j = 6-12$  transitions. The QM data are for spin-orbit conserving  $f-f$  transitions, while the QCT calculations are inherently closed shell. For the transitions shown,  $\Delta j =$  even are parity-conserving, while  $\Delta j =$  odd are parity-changing. The error bars on the experimental data represent the 95% confidence limits. Note that the classical limits of the orientation PP are  $-1 \leq a_{1-}^{(1)} \leq +1$ .

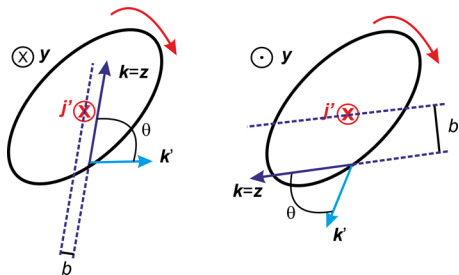


**Figure 8.** Two classical trajectories leading to scattering for the same  $\Delta j$  and scattering angle,  $\theta$ , but leading to equal and opposite rotational angular momentum orientation. The trajectory on the left induces rotational polarization along  $-y$ , while that on the right induces polarization along  $+y$ , with the net effect that there is no orientation in the classical hard shell model.

zero. It is clear from the n-PDPCSS that high impact parameter 518 collisions result in negative orientation, whereas positive 519 orientation results from collisions at smaller impact parameters. 520

*Classical Full and Soft Potential Calculations.* As discussed 521 above, in the case of classical hard shell collisions, the number 522 of trajectories leading to positive orientation is equal to that 523 leading to negative orientation. However, when considering the 524 full potential, attractive and soft repulsive parts of the 525 interaction potential perturb the classical hard shell trajectories, 526 and the balance between the positive and negative orienting 527 trajectories is disrupted, resulting in nonvanishing rotational 528 orientation. As a consequence, in general there will be collision- 529 induced rotational orientation if a finite range potential acts on 530 the classical system.<sup>7</sup>

If the interaction is governed by the full potential, as shown 532 in the top panels of Figure 10, the symmetry of the  $(-)$  and  $(+)$  533 orientation resolved normalized PDDCSs,  $n_{1-}^{(1)}(\theta)$ , is broken for 534 almost all scattering angles and final states. For low  $\Delta j$  535 transitions, a positive peak is observed at small scattering 536 angles, as shown in the left panel of Figure 10. This is due to 537 the long-range attractive forces, which result in an anticlockwise 538 sense of rotation. This is confirmed by the orientation resolved 539 n-PDPCSS, where the main positive contribution to the 540 orientation is found at impact parameters between 3.5 and 541 5.5 Å, for which trajectories mostly sample the attractive well. 542 The mechanism responsible for the positive orientation, i.e.,  $j'$  543 along  $+y$ , can be summarized as follows: for large enough 544 impact parameters, the collisions take place on the attractive 545 part of the potential. As the atom passes by the diatom, it is 546 deflected to the far side of the molecule. The diatom rotates in 547 the direction of the departing atom because of the attractive 548 nature of the interaction. Therefore, the rotational orientation 549 will be positive in the scattering frame. The attractive well is less 550 capable of inducing transitions to higher  $j'$  states; thus, this 551 mechanism gradually becomes less prominent and disappears 552 for  $\Delta j \gtrsim 3$ . For transitions in the range  $\Delta j \approx 5-7$ , attractive and 553 repulsive forces nearly balance each other, leading to small net 554 rotational orientation, as shown in the middle panel of Figure 555 10.<sup>7</sup>

Naively, one might expect that the orientation vanishes as the 557 collision becomes more impulsive, or hard shell like, with 558 increasing  $\Delta j$ ; however, this is clearly not the case. The overall 559 rotational orientation gradually becomes more negative, i.e.,  $j'$  560 along  $-y$ , for high  $\Delta j$  transitions as a consequence of the 561 lessening weight of the  $(+)$   $n_{1-}^{(1)}(\theta)$  orientation resolved 562 PDDCS with respect to its negative counterpart, shown in 563 the rightmost columns of Figure 10.<sup>564</sup>

The roles of the attractive and repulsive forces can be further 565 explored by comparing calculations performed using the full 566 and soft repulsive potentials. The purely repulsive soft potential 567 was constructed using eqs 13 and 14. The  $(+)$  and  $(-)$  568 orientation resolved PDDCSs almost perfectly cancel each 569 other for low  $\Delta j$  transitions, recovering the classical hard shell 570 case, as shown in the left panels of Figure 11. For high  $\Delta j$  571 transitions, the total and orientation resolved PDDCSs and n- 572 PDPCSS are similar to those obtained employing the full 573 potential, as can be concluded from the comparison of the right 574 panels of Figures 10 and 11. There is a clear propensity for 575 collisions that result in high rotational excitation to lead to 576 negative, or clockwise, final rotational orientation. This implies 577 that in the case of real collisions on the full potential, repulsive 578 forces are responsible for the rotational orientation in the case 579 of high rotational excitation. However, note that the repulsive 580

8. As discussed further below, the symmetry of such encounters 497 may be removed by secondary hard shell collisions with the 498 diatom,<sup>2,45</sup> giving rise to net rotational orientation.

9. Figure 9 displays the  $\rho_{1-}^{(1)}(\theta)$  renormalized PDDCSs, and the 499 500  $n_{1-}^{(1)}(\theta)$  normalized PDDCSs, obtained from classical hard shell 501 502 calculations for a selection of final states, resolved into those 503 504 which result in positive  $(+)$  and negative  $(-)$  orientation. Here, 505 506 the symmetry between collisions resulting in positive and 507 508 negative orientation can clearly be seen. The total normalized 509 510 orientation PDDCSs,  $n_{1-}^{(1)}(\theta)$ , is the sum of the two orientation 511 512 resolved PDDCSs; hence, it vanishes for all scattering angles 513 514 and final states, resulting in no net orientation. The double- 515 516 peaked structure in the  $n_{1-}^{(1)}(\theta)$  PDDCS reflects the angular 517 518 distribution of the scattered products.

10. Orientation resolved normalized polarization-dependent 519 partial cross sections, n-PDPCSS, are also shown in the bottom 520 row of Figure 9, in which the final rotational orientation is 521 plotted as a function of the initial impact parameter,  $b$ . The 522 n- 523 PDPCSS are obtained using eq 12. As shown in the figure, the 524 525 positive and negative contributions to the total n-PDPCSS do 526 527 not cancel out at each impact parameter; however, when 528 529 integrated over all impact parameters, the net orientation is 530 531

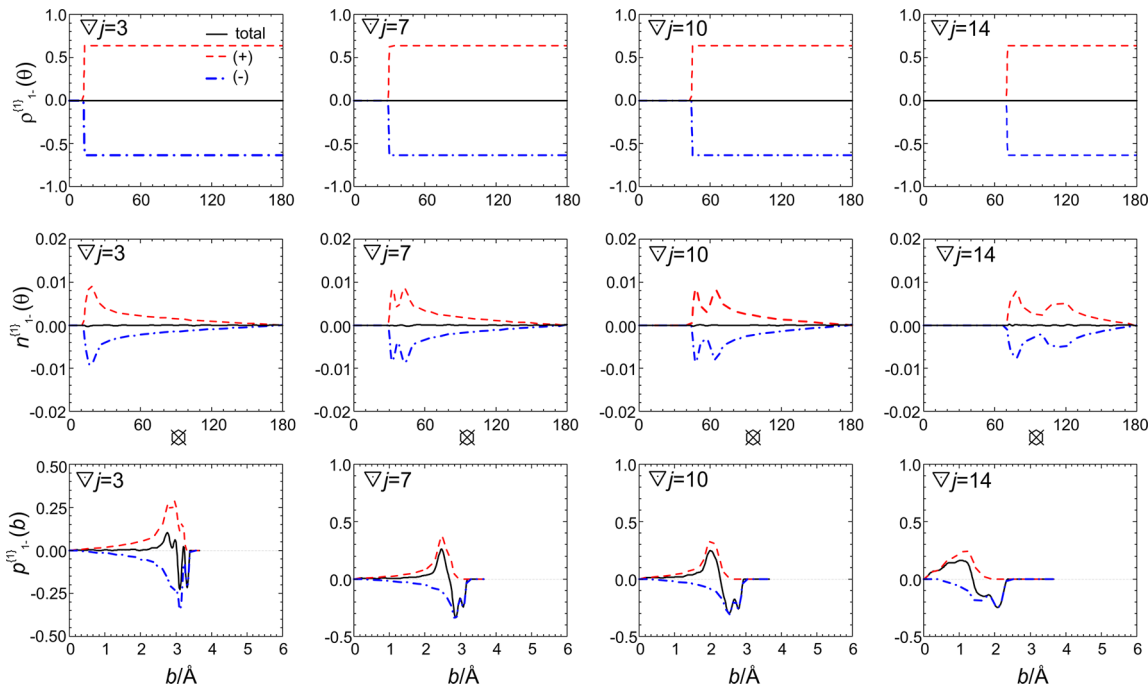


**Figure 9.** Top row: classical hard shell total (black solid line) and orientation resolved renormalized PDDCSs ((+) red dashed line, (−) blue dash-dotted line),  $\rho_{1\pm}^{(1)}(\theta)$ . Middle row: total and normalized PDDCSs,  $n_{1\pm}^{(1)}(\theta)$ . Bottom row: orientation resolved n-PDPCSSs,  $p_{1\pm}^{(1)}(b)$  (see text for its definition). The different columns correspond to the  $\Delta j = 3, 7, 10$ , and 14 transitions from left to right.

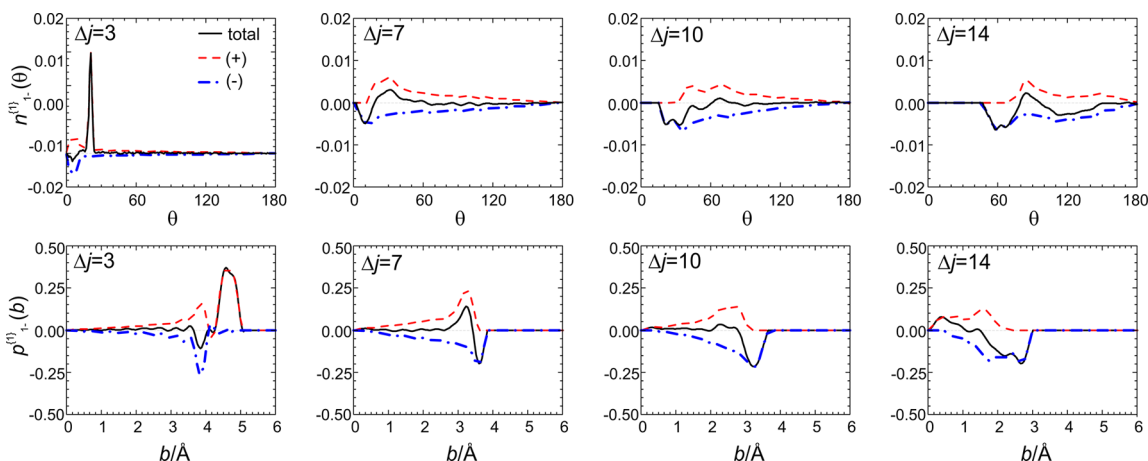


**Figure 10.** QCT total (black solid line) and orientation resolved normalized PDDCSs ((+) red dashed line, (−) blue dash-dotted line),  $n_{1\pm}^{(1)}(\theta)$  employing the full  $V_{\text{sum}}(R, \gamma)$  potential are shown in the top row for the  $\Delta j = 3, 7, 10$ , and 14 transitions from left to right. The corresponding total and orientation resolved n-PDPCSSs,  $p_{1\pm}^{(1)}(b)$ , are shown in the bottom row.

881 interaction must operate over a finite range for the collision-  
882 induced orientation to be observed in classical calculations.

883 Two limiting classical mechanisms causing collision-induced  
884 rotational orientation have thus been identified.<sup>7</sup> For low  $\Delta j$   
885 transitions, long-range attractive forces deflect the atom to the  
886 far side resulting in positive rotational orientation. For high  $\Delta j$   
887 transitions, the short-range repulsive forces repel those atoms  
888 that approach the diatom at shallow Jacobi angles and would  
889 otherwise lead to positive rotational orientation. As a  
890 consequence, the rotational orientation is negative.

891 As a final remark, the definition and the possible role of the  
892 chattering collisions<sup>8,45</sup> should be clarified. In the case of hard  
893 shell scattering, a collision is called chattering if the atom suffers  
894 an encounter with the diatom multiple times. We did not find  
895 any evidence for this type of collision using the exact hard shell

contour at a collision energy of  $530 \text{ cm}^{-1}$  (66 meV). If the interaction potential is smooth, a chattering collision refers to an event where the final rotational angular momentum is lower than the maximum rotational angular momentum achieved during collision.<sup>8</sup> Because the interaction is continuous, it can be considered as a prolonged interaction rather than a sequence of two separate collisions. To conclude, we do not believe that chattering collisions are responsible for the pronounced orientation observed on either the full, the soft, or hard shell PESs under the present collision energy conditions. Indeed, on the contrary, there is evidence that chattering collisions in NO(X) + Ar can lead to a decrease in the orientation and alignment of the final rotational angular momentum.<sup>8</sup>

**Quantum Mechanical Collisions. Closed Shell Calculations on the Soft Repulsive and Full PESs.** Closed shell

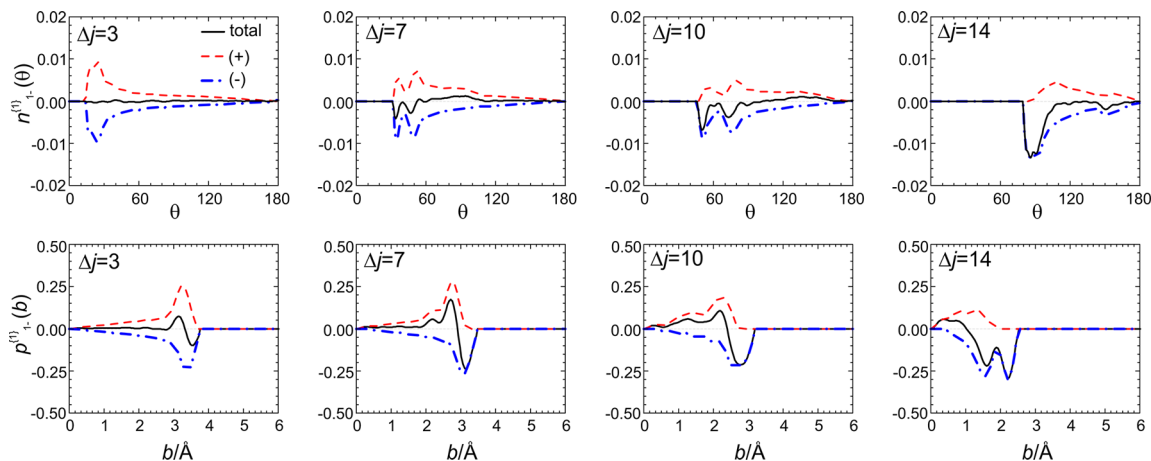


**Figure 11.** QCT total (black solid line) and orientation resolved normalized PDDCSs ((+) red dashed line, (−) blue dash-dotted line),  $n_{1-}^{(1)}(\theta)$  employing the purely repulsive  $V_{\text{sum}}(R, \gamma)$  potential are shown in the top row for the  $\Delta j = 3, 7, 10$ , and 14 transitions from left to right. The corresponding total and orientation resolved n-PDPCSSs,  $p_{1-}^{(1)}(b)$ , are shown in the bottom row.

611 quantum mechanical calculations were performed on the soft  
612 repulsive  $V_{\text{sum}}(R, \gamma)$  potentials. Closed shell, close-coupled  
613 renormalized  $\rho_{1-}^{(1)}(\theta)$  PDDCSs calculated using the full and  
614 “soft” potentials, as well as those obtained with the QM hard  
615 shell approximation are compared in Figure 12 for the indicated

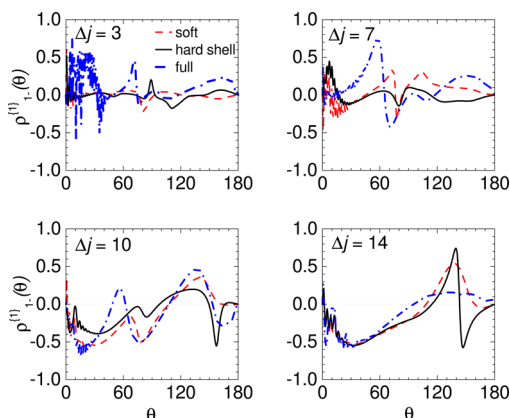


**Figure 12.** Hard shell QM (black solid line), soft potential CC QM (red dashed line), and full potential (blue dash-dotted line) renormalized PDDCSs,  $\rho_{1-}^{(1)}(\theta)$ , for the indicated  $\Delta j$  transitions.

616  $\Delta j$  transitions. The QM calculated orientation moments on the  
617 full, soft, and hard shell PESs all show a number of features in  
618 common, which are not present in the classical calculations. All  
619 show changes in sign of orientation as a function of scattering  
620 angle, although the precise angles at which these sign changes  
621 occur varies somewhat with choice of PES. Furthermore, at  
622 small scattering angles, the orientation moments display rapid  
623 diffraction-type oscillations. These oscillations are more evident  
624 for small  $\Delta j$  transitions. These rapid diffraction-type  
625 oscillations are not observed in the present experiments  
626 because the latter are of insufficient angular resolution.  
627 The classical roles of the attractive and repulsive features of  
628 the  $V_{\text{sum}}(R, \gamma)$  potential can easily be recognized in the QM  
629 orientation data. A positive orientation lobe is observed in the  
630 forward scattered region for low  $\Delta j$  collisions in the case of the  
631 full potential, for which the attractive region of the PES is  
632 present. This feature is absent in the “soft” potential and hard  
633 shell cases, showing that the attraction is responsible for the

positive orientation for these low final rotational states. The  
634 three calculations differ mostly for the medium  $\Delta j$  transitions,  
635 whereas the results are very similar for high rotational  
636 excitation. As a matter of fact, the rotational orientation is  
637 virtually completely determined by the hard shell interaction for  
638  $\Delta j > 14$ .

**Quantum Mechanical Hard Shell Collisions.** The details of  
640 the QM hard shell calculations were discussed in [QM Close-](#)  
641 [Coupled Calculations](#). They provide an important benchmark  
642 for the current study. Unlike the classical collisions of hard shell  
643 atoms and molecules, which do not give rise to any collision-  
644 induced orientation, QM collisions between hard shell species  
645 generally do result in rotational orientation.<sup>7</sup> The orientation  
646 observed in the hard shell QM case arises from the nonlocal  
647 nature of the quantum mechanical interactions.<sup>7</sup> The incoming  
648 atom interacts with the diatom over a finite region of the hard  
649 shell potential, determined by the de Broglie wavelength of the  
650 system. There is no well-defined point of contact, leading to the  
651 breakdown of the rotational symmetry about the surface normal  
652 that was responsible for the lack of rotational orientation  
653 observed in classical hard shell collisions.<sup>7</sup> Furthermore, the  
654 interaction also takes place over a finite lapse of time, during  
655 which the diatom rotates. This invalidates one of the classical  
656 hard shell requirements for vanishing rotational orientation,  
657 namely, the interaction should happen in an infinitely short  
658 period of time. This point can be demonstrated by artificially  
659 reducing the rotational constant of the NO(X) molecule,  
660 thereby making it rotate more slowly. This results in a  
661 reduction in the calculated collision-induced rotational  
662 orientation, as demonstrated in the top row of Figure 13.

Conversely, longer de Broglie wavelengths are expected to be  
664 associated with stronger collision-induced rotational orienta-  
665 tion, because the interaction becomes less localized on the  
666 molecular surface.<sup>7</sup> This can be demonstrated by carrying out a  
667 series of calculations in which the reduced mass of the system is  
668 decreased by a factor of 4 and 64, in order to lengthen its de  
669 Broglie wavelength by a factor of 2 and 8, respectively. The  
670 longer the de Broglie wavelength, the more strongly  $j'$  is  
671 oriented, as seen in the bottom row of Figure 13.<sup>7</sup>

The QM hard shell mechanism is unique in the sense that it  
673 has no classical counterpart. It arises purely because of the  
674 quantum mechanical nature of the interaction.<sup>7</sup> It is expected  
675 that this QM mechanism will play a dominant role in collisions

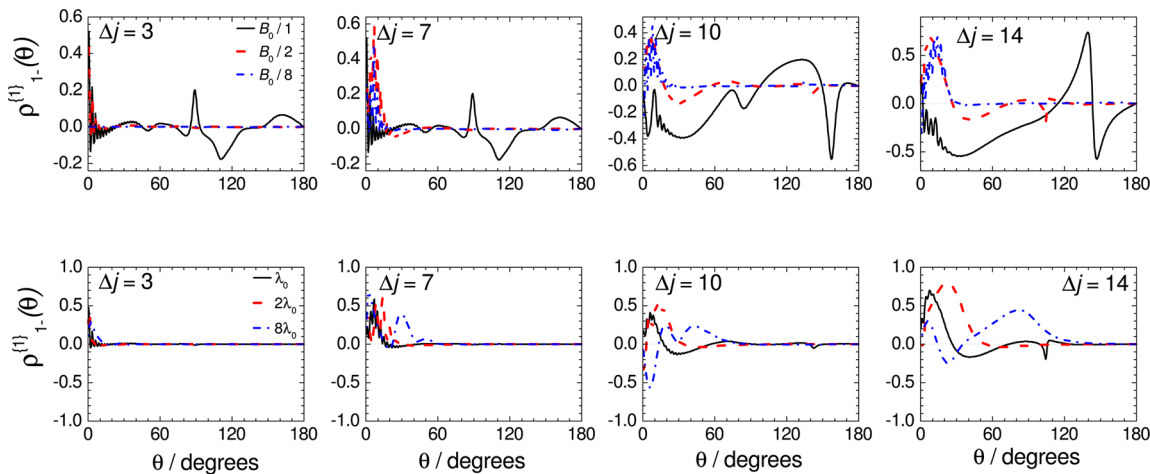


**Figure 13.** Closed shell hard shell QM calculations of the renormalized PDDCS,  $\rho_{1-}^{(1)}(\theta)$ , for the  $\Delta j = 3, 7, 10$ , and  $14$  transitions, showing the dependence of the orientation on the rotational constant (top row) and on the de Broglie wavelength (bottom row). Top row: unscaled,  $B_0$  (black solid line),  $B_0/2$  (red dashed line), and  $B_0/8$  (blue dash-dotted line). Bottom row: de Broglie wavelength unscaled,  $\lambda_0$  (black solid line),  $2\lambda_0$  (red dashed line), and  $8\lambda_0$  (blue dash-dotted line). For the calculations presented in the bottom row, the rotational constant was set to  $B_0/2$ .

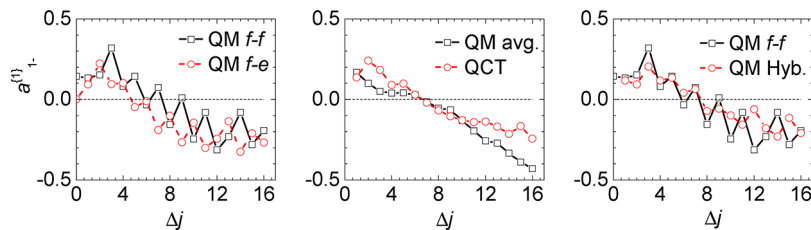


**Figure 14.** Left panel: the CC QM orientation moments for the  $|j, 0.5, -1\rangle \rightarrow |j', 0.5, -1\rangle$  ( $f-f$ ) transitions (black open squares) and for the  $|j, 0.5, -1\rangle \rightarrow |j', 0.5, +1\rangle$  ( $f-e$ ) transitions (red open circles). Middle panel: comparison of the CC QM orientation moments summed over the final and averaged over the initial  $\Lambda$ -doublet levels (black open squares) and QCT orientation moments (red open circles). Right panel: the CC QM (black open squares) and hybrid (red open circles) orientation moments for the  $|j, 0.5, -1\rangle \rightarrow |j', 0.5, -1\rangle$  transitions. Note that the classical limits of the orientation PP are  $-1 \leq a_{1-}^{(1)} \leq +1$ .

in which the interaction potential is steeply repulsive, such as in the collisions of NO(X) with He or Ne.

**Integral Orientation Moments.** As observed experimentally, the  $\Lambda$ -doublet resolved QM  $a_{1-}^{(1)}$  moments, obtained using eq 7, show a decreasing trend in orientation with increasing  $\Delta j$ , superimposed with parity-dependent oscillations (see the left panel of Figure 14). The phase of the oscillations is opposite for transitions to final  $f$  and  $e$  states, such that parity-conserving transitions display a more negative (or less positive) orientation than those for parity-changing collisions. Closed shell QCT orientation moments are compared with QM  $a_{1-}^{(1)}$  moments, which have been summed over initial and averaged final  $\Lambda$ -doublet level, in the middle panel of Figure 14. Both QCT and the summed and averaged QM moments show the same general trend, with  $a_{1-}^{(1)}$  decreasing with increasing rotational excitation. The good agreement between these two sets of orientation moments suggests that the QM orientation can partly be accounted for in terms of the classical “attractive” and “soft repulsive” mechanisms discussed in **Rotational Orientation in Classical Collisions**.

The  $\Delta j$ -dependent oscillations that are evident in the  $\Lambda$ -doublet resolved QM data are not seen for the QCT calculations. Such oscillations can be a result of parity-dependent differences in the QM DCSs or due to the PDDCSs themselves. The origin of these oscillations can be explored by considering the “hybrid” orientation PP, displayed in the right-hand panel of Figure 14. These hybrid orientation PPs are

constructed by integrating the product of the QCT renormalized PDDCSs,  $[\rho_{1-}^{(1)}(\theta)]_{\text{QCT}}$ , and the QM  $\Lambda$ -doublet resolved angular distribution,  $[n_0^{(0)}(\theta)]_{\text{QM}}$ , over  $\cos \theta$ , i.e.

$$\begin{aligned} [a_{1-}^{(1)}]_{\text{hybrid}} &= \int d\cos \theta [n_0^{(1)}]_{\text{hybrid}} \\ &= \int d\cos \theta [\rho_{1-}^{(1)}(\theta)]_{\text{QCT}} [n_0^{(0)}(\theta)]_{\text{QM}} \end{aligned} \quad (16)$$

While the hybrid PPs reproduce the decreasing trend in orientation with increasing  $\Delta j$  reasonably well, they fail to follow the oscillations seen in the  $f-f$  QM orientation moments. The oscillations in the  $\Lambda$ -doublet resolved  $a_{1-}^{(1)}$  moments must thus be a result of parity-dependent differences in the polarization behavior itself. In a previous study of the NO(X) + Ar system, analogous “hybrid” alignment moments were able to reproduce very well the QM  $\Lambda$ -doublet resolved data.<sup>3</sup> This reflects the underlying classical nature of rotational alignment, whereas the collision-induced rotational orientation is clearly significantly influenced by quantum mechanical effects, as discussed in **QM Hard Shell Calculations**.

## CONCLUSIONS

The rotational orientation after collisions of fully  $\Lambda$ -doublet state selected NO(X) with Ar has been investigated. Experimental normalized,  $n_{1-}^{(1)}(\theta)$ , and renormalized,  $\rho_{1-}^{(1)}(\theta)$ , polarization-dependent differential cross sections and integral

726 polarization parameters,  $a_1^{[1]}$ , have been compared with CC  
 727 QM calculations and are found to be in very good agreement.  
 728 In contrast, simulations performed using QCT calculations  
 729 were unable to reproduce the orientation observed exper-  
 730 imentally or in the QM simulations.

731 The origins of the rotational orientation generated in the  
 732 collisions of NO(X) and Ar at a collisions energy of  $530\text{ cm}^{-1}$   
 733 (66 meV) have also been investigated theoretically. Classical  
 734 and quantum mechanical calculations have been used to  
 735 demonstrate the effect of the attractive and soft repulsive parts  
 736 of the potential on the rotational orientation, in comparison to  
 737 collisions of hard shell species. For classical collisions, the  
 738 symmetry of the collision of a hard shell results in no net  
 739 rotational orientation. This symmetry is removed when a finite-  
 740 range interaction potential is present.<sup>7</sup> For collisions that take  
 741 place on a soft repulsive potential, predominantly negative  
 742 orientation is observed. In the presence of the full potential,  
 743 clear features of the attractive region of the potential can be  
 744 identified at low rotational excitation, leading to positive  
 745 orientation. These two observations are in agreement with the  
 746 limiting classical mechanisms proposed previously.<sup>5,7,11</sup>

747 In contrast to the classical behavior, quantum mechanical  
 748 encounters between hard shell molecules and atoms can also  
 749 lead to collision-induced rotational orientation. This purely  
 750 quantum mechanical effect arises because of the inherent  
 751 nonlocal nature and finite duration time of the QM collision  
 752 encounter.<sup>7</sup> The QM mechanism for collision-induced rota-  
 753 tional orientation is shown to play a significant role in the  
 754 inelastic scattering of NO by Ar, particularly at high  $\Delta j$ , for  
 755 which the collisions become more impulsive in nature.

## 756 ■ AUTHOR INFORMATION

### 757 Corresponding Authors

758 \*E-mail: mark.brouard@chem.ox.ac.uk.

759 \*E-mail: aoiz@quim.ucm.es.

760 \*E-mail: stolte@chem.vu.nl.

### 761 Present Addresses

762 <sup>§</sup>H.C.: Laboratoire de Chimie Physique Moléculaire, Ecole  
 763 Polytechnique Fédérale de Lausanne, Lausanne, Switzerland.

764 <sup>||</sup>B.H.: School of Chemistry, University of Bristol, Cantock's  
 765 Close, Bristol BS8 1TS, United Kingdom.

### 766 Notes

767 The authors declare no competing financial interest.

## 768 ■ ACKNOWLEDGMENTS

769 The support of the UK EPSRC (to M.B. via Programme Grant  
 770 EP/L005913/1), the EU (to M.B. via FP7 EU People ITN  
 771 Project 238671), and the Spanish Ministry of Science and  
 772 Innovation (Grants CTQ2012-37404 and CSD2009-00038, to  
 773 F.J.A.) are gratefully acknowledged. S.S. acknowledges support  
 774 from the National Basic Research Program of China (973  
 775 program) under Grant 2013CB922200, and from the National  
 776 Science Foundation of China under Grants 11034003 and  
 777 91221301. S.D.S.G. and M.B. also thank Cambio Ltd. and Dr.  
 778 Peter Dean for generous support.

## 779 ■ REFERENCES

- (1) Kim, S. K.; Herschbach, D. R. Angular Momentum Disposal in Atom Exchange Reactions. *Faraday Discuss. Chem. Soc.* **1987**, *84*, 159.
- (2) Cline, J. I.; Lorenz, K. T.; Wade, E. A.; Barr, J. W.; Chandler, D. W. Ion imaging measurement of collision-induced rotational alignment in Ar-NO scattering. *J. Chem. Phys.* **2001**, *115*, 6277.

- (3) Brouard, M.; Chadwick, H.; Eyles, C. J.; Hornung, B.; Nichols, B.; Aoiz, F. J.; Jambrina, P. G.; Stolte, S.; de Miranda, M. P. Rotational alignment effects in NO(X) + Ar inelastic collisions: A theoretical study. *J. Chem. Phys.* **2013**, *138*, 104309.
- (4) Brouard, M.; Chadwick, H.; Eyles, C. J.; Hornung, B.; Nichols, B.; Aoiz, F. J.; Jambrina, P. G.; Stolte, S. Rotational alignment effects in NO(X) + Ar inelastic collisions: An experimental study. *J. Chem. Phys.* **2013**, *138*, 104310.
- (5) Alexander, M. H. Close-coupling studies of orientation dependence of rotationally inelastic collisions. *J. Chem. Phys.* **1977**, *67*, 2703.
- (6) Lorenz, K. T.; Chandler, D. W.; Barr, J. W.; Chen, W.; Barnes, G. L.; Cline, J. I. Direct measurement of the preferred sense of NO rotation after collision with argon. *Science* **2001**, *293*, 2063.
- (7) Brouard, M.; Hornung, B.; Aoiz, F. J. Origin of collision-induced molecular orientation. *Phys. Rev. Lett.* **2013**, *111*, 183202.
- (8) Aoiz, F. J.; Herrero, V. J.; Rábano, V. S.; Verdasco, J. E. Classical stereodynamics in Ar plus NO inelastic collisions. *Phys. Chem. Chem. Phys.* **2004**, *6*, 4407.
- (9) Jambrina, P. G.; Klos, J.; Aoiz, F. J.; de Miranda, M. P. New findings regarding the NO angular momentum orientation in Ar-NO( $^2\Pi_{1/2}$ ) collisions. *Phys. Chem. Chem. Phys.* **2012**, *14*, 9826.
- (10) Aoiz, F. J.; Brouard, M.; Enriquez, P. A. Product rotational polarization in photon-initiated bimolecular reactions. *J. Chem. Phys.* **1996**, *105*, 4964.
- (11) Aoiz, F. J.; Brouard, M.; Herrero, V. J.; Rabano, V. S.; Stark, K. Product rotational polarization. The stereodynamics of the F + H<sub>2</sub> reaction. *Chem. Phys. Lett.* **1997**, *264*, 487–494.
- (12) de Miranda, M. P.; Aoiz, F. J.; Bañares, L.; Rábano, V. S. A unified quantal and classical description of the stereodynamics of elementary chemical reactions: State-resolved  $k \cdot k' \cdot j'$  vector correlation for the H + D<sub>2</sub>( $v = 0, j = 0$ ) reaction. *J. Chem. Phys.* **1999**, *111*, 5368.
- (13) Aldegunde, J.; Aoiz, F. J.; González-Sánchez, L.; Jambrina, P. G.; de Miranda, M. P.; Sáez-Rábano, V. Orientation effects in Cl + H<sub>2</sub> inelastic collisions: characterization of the mechanisms. *Phys. Chem. Chem. Phys.* **2012**, *14*, 2911–2920.
- (14) Rakitzis, T. P.; Kandel, S. A.; Lev-On, T.; Zare, R. N. Differential cross section polarization moments: Location of the D-atom transfer in the transition-state region for the reactions Cl + C<sub>2</sub>D<sub>6</sub> → DCl( $v' = 0, j' = 1$ ) + C<sub>2</sub>D<sub>5</sub> and Cl + CD<sub>4</sub> → DCl( $v' = 0, j' = 1$ ) + CD<sub>3</sub>. *J. Chem. Phys.* **1997**, *107*, 9392–9405.
- (15) Chadwick, H.; Nichols, B.; Gordon, S. D. S.; Hornung, B.; Squires, E.; Brouard, M.; Klos, J.; Alexander, M. H.; Aoiz, F. J.; Stolte, S. Inelastic Scattering of NO by Kr: Rotational Polarization over a Rainbow. *J. Phys. Chem. Lett.* **2014**, *5*, 3296–3301.
- (16) Alexander, M. H. Rotationally inelastic collisions between a diatomic molecule in a  $^2\Pi$  electronic state and a structureless target. *J. Chem. Phys.* **1982**, *76*, 5974.
- (17) Alexander, M. H. Quantum treatment of rotationally inelastic collisions involving molecules in  $\Pi$ -electronic states - new derivation of the coupling potential. *Chem. Phys.* **1985**, *92*, 337.
- (18) Alexander, M. H. Differential and integral cross-sections for the inelastic scattering of NO( $X^2\Pi$ ) by Ar on a new ab initio potential energy surface. *J. Chem. Phys.* **1993**, *99*, 7725.
- (19) Alexander, M. H. A new, fully *ab initio* investigation of the NO( $X^2\Pi$ )Ar system. I. Potential energy surfaces and inelastic scattering. *J. Chem. Phys.* **1999**, *111*, 7426.
- (20) Suits, A. G.; Bontyan, L. S.; Houston, P. L.; Whitaker, B. J. Differential cross-sections for the state-selected products by direct imaging - Ar + NO. *J. Chem. Phys.* **1992**, *96*, 8618.
- (21) Jons, S. D.; Shirley, J. E.; Vonk, M. T.; Giese, C. F.; Gentry, W. R. State-to-state differential cross-sections for rotationally inelastic multiplet-conserving and multiplet-changing collisions of NO ( $^2\Pi_{1/2}, j = 0.5$ ) with Ar. *J. Chem. Phys.* **1992**, *97*, 7831.
- (22) Jons, S. D.; Shirley, J. E.; Vonk, M. T.; Giese, C. F.; Gentry, W. R. State-to-state differential cross sections for rotationally inelastic collisions of NO( $^2\Pi_{1/2}, j = 0.5$ ) with Ar at kinetic energies between 117 cm<sup>-1</sup> and 1694 cm<sup>-1</sup>. *J. Chem. Phys.* **1996**, *105*, 5397.

- 853 (23) Bontyan, L. S.; Suits, A. G.; Houston, P. L.; Whitaker, B. J.  
 854 State-resolved differential cross-sections for the crossed-beam Ar-NO  
 855 inelastic-scattering by direct ion imaging. *J. Phys. Chem.* **1993**, *97*,  
 856 6342.
- 857 (24) Eliooff, M. S.; Chandler, D. W. State-to-state differential cross  
 858 sections for spin-multiplet-changing collisions of NO( $X^2\Pi_{1/2}$ ) with  
 859 argon. *J. Chem. Phys.* **2002**, *117*, 6455.
- 860 (25) Aoiz, F. J.; Verdasco, J. E.; Herrero, V. J.; Rábano, V. S.;  
 861 Alexander, M. H. Attractive and repulsive interactions in the inelastic  
 862 scattering of NO by Ar: A comparison between classical trajectory and  
 863 close-coupling quantum mechanical results. *J. Chem. Phys.* **2003**, *119*,  
 864 5860.
- 865 (26) Eyles, C. J.; Brouard, M.; Yang, C.-H.; Klos, J.; Aoiz, F. J.;  
 866 Gijsbertsen, A.; Wiskerke, A. E.; Stolte, S. Interference structures in the  
 867 differential cross-sections for inelastic scattering of NO by Ar. *Nat. Chem.* **2011**, *3*, 597.
- 868 (27) Eyles, C. J.; Brouard, M.; Chadwick, H.; Hornung, B.; Nichols,  
 869 B.; Yang, C.-H.; Klos, J.; Aoiz, F. J.; Gijsbertsen, A.; Wiskerke, A. E.;  
 870 et al. Fully lambda-doublet resolved state-to-state differential cross-  
 872 sections for the inelastic scattering of NO(X) with Ar. *Phys. Chem. Chem.*  
 873 *Phys.* **2012**, *14*, 5403.
- 874 (28) Eyles, C. J.; Brouard, M.; Chadwick, H.; Aoiz, F. J.; Klos, J.;  
 875 Gijsbertsen, A.; Zhang, X.; Stolte, S. The effect of parity conservation  
 876 on the spin-orbit conserving and spin-orbit changing differential cross  
 877 sections for the inelastic scattering of NO(X) by Ar. *Phys. Chem. Chem.*  
 878 *Phys.* **2012**, *14*, 5420.
- 879 (29) von Zastrow, A.; Onvlee, J.; Vogels, S. N.; Groenenboom, G. C.;  
 880 van der Avoird, A.; van de Meerakker, S. Y. T. State-resolved  
 881 diffraction oscillations imaged for inelastic collisions of NO radicals  
 882 with He, Ne and Ar. *Nat. Chem.* **2014**, *6*, 216–221.
- 883 (30) Vogels, S. N.; Onvlee, J.; von Zastrow, A.; Groenenboom, G. C.;  
 884 van der Avoird, A.; van de Meerakker, S. Y. T. High-Resolution  
 885 Imaging of Velocity-Controlled Molecular Collisions Using Counter-  
 886 propagating Beams. *Phys. Rev. Lett.* **2014**, *113*, 263202.
- 887 (31) Onvlee, J.; Vogels, S. N.; van der Avoird, A.; Groenenboom, G.  
 888 C.; van de Meerakker, S. Y. T. Resolving rainbows with superimposed  
 889 diffraction oscillations in NO plus rare gas scattering: experiment and  
 890 theory. *New J. Phys.* **2015**, *17*, 055019.
- 891 (32) Wade, E. A.; Lorenz, K. T.; Chandler, D. W.; Barr, J. W.; Barnes,  
 892 G. L.; Cline, J. I. Ion imaging studies of product rotational alignment in  
 893 collisions of NO ( $X^2\Pi_{1/2}, j = 0.5$ ) with Ar. *Chem. Phys.* **2004**, *301*, 261.
- 894 (33) Gijsbertsen, A.; Linnartz, H.; Rus, G.; Wiskerke, A. E.; Stolte, S.;  
 895 Chandler, D. W.; Klos, J. Differential cross sections for collisions of  
 896 hexapole state-selected NO with He. *J. Chem. Phys.* **2005**, *123*, 224305.
- 897 (34) Eppink, A. T. J. B.; Parker, D. H. Velocity map imaging of ions  
 898 and electrons using electrostatic lenses: Application in photoelectron  
 899 and photofragment ion imaging of molecular oxygen. *Rev. Sci. Instrum.*  
 900 **1997**, *68*, 3477.
- 901 (35) Chandler, D. W.; Houston, P. L. Two-dimensional imaging of  
 902 state-selected photodissociation products detected by multiphoton  
 903 ionization. *J. Chem. Phys.* **1987**, *87*, 1445.
- 904 (36) Alexander, A. J. Determination of the helicity of oriented  
 905 photofragments. *J. Chem. Phys.* **2005**, *123*, 194312.
- 906 (37) Brouard, M.; Chadwick, H.; Gordon, S. D. S.; Hornung, B.;  
 907 Nichols, B.; Klos, J.; Aoiz, F. J.; Stolte, S. Fully quantum state-resolved  
 908 inelastic scattering of NO (X)+ Kr: Differential cross sections and  
 909 product rotational alignment. *J. Chem. Phys.* **2014**, *141*, 164306.
- 910 (38) Aldegunde, J.; de Miranda, M. P.; Haigh, J. M.; Kendrick, B. K.;  
 911 Sáez-Rábano, V.; Aoiz, F. J. How reactants polarization can be used to  
 912 change and unravel chemical reactivity. *J. Phys. Chem. A* **2005**, *109*,  
 913 6200–6217.
- 914 (39) Hertel, I. V.; Stoll, W. Collision experiments with laser excited  
 915 atoms in crossed beams. *Adv. At. Mol. Phys.* **1978**, *13*, 113.
- 916 (40) Alexander, M. H. Propensity rules for rotationally inelastic  
 917 collisions of symmetric top molecules or linear polyatomic molecules  
 918 with structureless atoms. *J. Chem. Phys.* **1982**, *77*, 1855.
- 919 (41) Brouard, M.; Chadwick, H.; Eyles, C. J.; Hornung, B.; Nichols,  
 920 B.; Scott, J. M.; Aoiz, F. J.; Klos, J.; Stolte, S.; Zhang, X. The fully  
 921 quantum state-resolved inelastic scattering of NO(X) + Ne: 921  
 922 experiment and theory. *Mol. Phys.* **2013**, *111*, 1759. 922
- 923 (42) Beck, D.; Ross, U.; Schepper, W. Rotationally inelastic, classical 923  
 924 scattering from an anisotropic rigid shell potential of rotation 924  
 925 symmetry. *Z. Phys. A: At. Nucl.* **1979**, *293*, 107. 925
- 926 (43) Buck, U.; Huisken, F.; Pauly, H.; Schleusener, J. Intermolecular 926  
 927 potentials by the inversion of differential cross sections. V. ArKr. *J. 927  
 928 Chem. Phys.* **1978**, *68*, 3334. 928
- 929 (44) Kreutz, T. G.; Flynn, G. W. Analysis of translationa;, rotational, 929  
 930 and vibrational-energy transfer in collision between CO<sub>2</sub> and hot 930  
 931 hydrogen-atoms - The 3-dimensional breathing ellipsoid model. *J. 931  
 932 Chem. Phys.* **1990**, *93*, 452. 932
- 933 (45) Bosanac, S. 2-dimensional model of rotationally inelastic 933  
 934 collisions. *Phys. Rev. A: At., Mol., Opt. Phys.* **1980**, *22*, 2617. 934
- 935 (46) Aoiz, F. J.; Herrero, V. J.; Rabanos, V. S. Quasiclassical state to 935  
 936 state reaction cross sections for D+H<sub>2</sub>(v = 0, j = 0) → HD(v<sub>j</sub>) + H. 936  
 937 Formation and characteristics of short-lived collision complexes. *J. 937  
 938 Chem. Phys.* **1992**, *97*, 7423. 938
- 939 (47) Bosanac, S. D.; Petrović, N. Quantum theory of impulsive 939  
 940 collisions. *Phys. Rev. A: At., Mol., Opt. Phys.* **1990**, *41*, 5909. 940
- 941 (48) Bosanac, S. D.; Murrell, J. N. Hard Shell potentials from 941  
 942 rotational state-to-state inelastic scattering - a possible route to 942  
 943 inversion. *J. Chem. Phys.* **1991**, *94*, 1167. 943
- 944 (49) HIBRIDON is a package of programs for the time-independent 944  
 945 quantum treatment of inelastic collisions and photodissociation 945  
 946 written by Alexander, M. H., Manopoulos, D. E., Werner, H.-J., 946  
 947 Follmeg, B., with contributions by Vohralík, P. F., Lemoine, D., Corey, 947  
 948 G., Gordon, R., Johnson, B., Orlowski, T., Berning, A., Degli-Esposti, 948  
 949 A., Rist, C., Dagdigian, P., Pouilly, B., van der Sanden, G., Yang, M., de 949  
 950 Weerd, F., Gregurick, S., Klos, J.. 950